ACS OMEGA

Article

Cite This: ACS Omega 2018, 3, 2183−2192

Microwave Permittivity of Trace sp^2 Carbon Impurities in Sub-Micron Diamond Powders

Jerome Alexander Cuenca,*[,†] Evan Lloyd Hunter Thomas,[‡] Soumen Mandal,[‡] David John Morgan,[§] Fernando Lloret,[∥] Daniel Araujo,[∥] Oliver Aneurin Williams,[‡] and Adrian Porch[†]

[†]School of Engineering and [‡]School of Physics and Astronomy, Cardiff University, Newport Road, Cardiff CF24 3AA, Wales, U.K.

[§]Cardiff Catalysis Institute, School of Chemistry, Cardiff University, Park Place, Cardiff, CF10 3AT Wales, U.K.

[∥]Departamento de Ciencias de los Materiales e Ingeniería Metalúrgica y Química, Universidad de Cádiz, 11510 Puerto Real, Cádiz, Spain

ABSTRACT: Microwave dielectric loss tangent measurements are demonstrated as a method for quantifying trace sp^2-hybridized carbon impurities in sub-micron diamond powders. Appropriate test samples are prepared by vacuum annealing at temperatures from 600 to 1200 °C to vary the sp^2/sp^3 carbon ratio through partial surface graphitization. Microwave permittivity measurements are compared with those obtained using X-ray photoelectron spectroscopy (XPS), Raman spectroscopy, and electron energy loss spectroscopy (EELS). The average particle size remains constant (verified by scanning electron microscopy) to decouple any geometric dielectric effects from the microwave measurements. After annealing, a small increase in sp^2 carbon was identified from the XPS C 1s and Auger spectra, the EELS σ^* peak in the C 1s spectra, and the D and G bands in Raman spectroscopy, although a quantifiable diamond to G-band peak ratio was unobtainable. Surface hydrogenation was also evidenced in the Raman and XPS O 1s data. Microwave cavity perturbation measurements show that the dielectric loss tangent increases with increasing sp^2 bonding, with the most pertinent finding being that these values correlate with other measurements and that trace concentrations of sp^2 carbon as small as 5% can be detected.

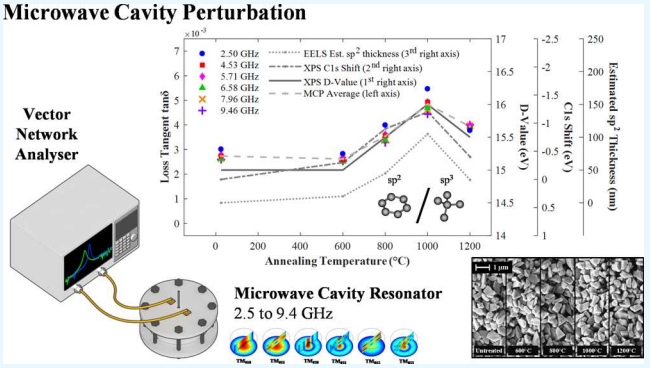

1. INTRODUCTION

Sub-micron diamonds allow the outstanding material characteristics of diamond relating to its electrical, thermal, chemical, and mechanical properties to be applied on microscopic scales. Some pertinent examples of this include transistors with excellent heat spreading,[1−3] chemically inert particles for drug delivery,[4−7] and mechanically stable micro-electro-mechanical system structures for nanoscale sensing applications.[8,9] However, as diamond gets smaller, the surface area increases, and so does the volume of any non-diamond surface content, hydrogen terminations, and disordered, sp^2, and non-diamond carbons in the well-known core−shell model.[10−12] Non-diamond functional group terminations are preferred for conjugating certain types of proteins,[13] however, reconstructed sp^2 carbon terminations are considered a hindrance as this causes particle agglomeration;[11,12,14] hence, there has been much research into rigorous purification methods.[15−17] Hence, characterization of non-diamond impurities on nano-diamond is a prominent research area for assessing its quality in various applications.

One of the most popular methods to examine diamond particles is X-ray photoelectron spectroscopy (XPS)because of its sensitivity to particle surfaces, its low sample volume requirement, and its ability to identify and infer carbon- and hydrogen-related terminations.[18] Carbon-based impurities can be identified in a number of ways, one of which is to observe the C 1s spectrum. For sp^3 carbon, the C 1s peak is observed at a higher binding energy than sp^2 carbon,[19−21] so one can obtain the sp^2/sp^3 carbon ratio either through observing shifts or by deconvolution of the two associated peaks. Although, the C 1s peak is generally used as a charge reference at 284.8 eV, associated with the thin layer of carbon that is formed when the sample is exposed to air (called the adventitious carbon peak), making any absolute shifts is difficult to determine. Furthermore, surface charging may shift the observed peak.[20] More effective methods use different regions of the XPS spectra, including the valence band region and the derivative of the C KLL Auger spectra.[10,22−24] Speranza and Laidani[22] showed that the latter case minimizes the referencing error in determining the sp^2/sp^3 carbon ratio because it is a differential technique using the eV difference in maxima and minima.

Another notable spectroscopic method is scanning transmission electron microscopy using electron energy loss spectroscopy (STEM−EELS). In a similar fashion to XPS,

Received: December 16, 2017
Accepted: January 26, 2018
Published: February 22, 2018

DOI: 10.1021/acsomega.7b02000
ACS Omega 2018, 3, 2183−2192

EELS is capable of probing both surface plasmons and inner core (C 1s) electrons. Bulk diamond exhibits a strong σ-plasmon peak at around 33 eV, with an additional surface plasmon at 22 eV. The π-plasmon peak in graphite is at a much lower energy loss of around 5−8 eV.[10,23] However, the latter feature is challenging to measure as it is close to the zero loss peak and depends upon the experimental setup. Easier to obtain experimentally is the carbon K-edge loss spectra, resulting from the excitation of C 1s electrons to vacant π^* and σ^* orbitals. The former lower energy state is related to sp^2 (reported between 285 and 290 eV), and the latter higher state is related to sp^3 (reported at greater than 289 eV).[10,25−27]

Other spectroscopic methods to measure amorphous impurities in nano-diamonds are challenging as the strong characteristic signatures from sp^3 carbon in high volume fractions effectively flood the spectrum. Prime examples of this include nuclear magnetic resonance (NMR) and Raman spectroscopy, where, respectively, the 36.3 ppm sp^3 peak dominates over the 130−160 ppm range for sp^2 carbon and the 1332 cm^{-1} diamond peak dominates the spectra over the broad D and G bands at around 1340 and 1580 cm^{-1}.[23,28,29] However, numerous methods have been used to desensitize the presence of sp^3 carbon; changing the excitation wavelengths further toward the infrared (IR) region in Raman spectroscopy reveals many other features,[30−32] and in other cases, increasing the sample exposure time increases the signal to noise ratio. For the inspection of trace amounts of sp^2 carbon impurities, the material probe needs to be *insensitive* to the crystalline structure of diamond.

Dielectric or impedance spectroscopy, which measures electrical conductivity and/or dielectric loss, is ideal in this case because the highly insulating nature of pure diamond implies that the dominant electrical contribution will be due to conducting impurities. Because there is such a large contrast in the electrical properties of sp^3 and sp^2 carbon, it is clear that their concentrations can be indirectly inferred. There is, however, a drawback to using impedance spectroscopy on powders (particularly in the dc to kHz frequency range), where electrodes that are in physical contact with the powdered samples are required.[33−35] Although impedance spectroscopy gives a wideband electrical response of the material, an additional fabrication stage is typically needed, such as incorporating the powder into a solid host material or producing films with electrodes fabricated in direct contact. However, one can extend the measurement toward MHz and GHz frequencies to perform microwave dielectric spectroscopy, whereby noncontact resonating structures can be used to infer the conductivity and dielectric properties of a material[36] even in the presence of varying temperatures and gas atmospheres.[37,38] In particular, microwave cavity perturbation (MCP) has been highlighted as a potential technique for the examination of nano-diamond impurities owing to its high precision and fast sample analysis (in minutes, including sample preparation), although, its lower limits for evaluating trace quantities of sp^2 are yet to be tested.[29,39,40]

MCP, unlike XPS, EELS, or Raman spectroscopy, is not a phase quantification technique and does not provide a fingerprint of the materials present. It is a technique that measures the complex permittivity and permeability of a material at microwave frequencies, typically using a hollow metal structure (the "cavity") with well-defined resonances over the bandwidth from 1 to 10 GHz. This is achieved by perturbing the electromagnetic fields of the resonant cavity mode with a volume of the sample and measuring the change in the resonant frequency and quality factor (Q = resonant frequency/−3 dB bandwidth). The dielectric and magnetic properties of the sample can be obtained through the first-order cavity perturbation equation for a porous powder sample[41]

$$\varepsilon_{\mathrm{eff},1} \approx 2\frac{\Delta f}{f_0}\frac{V_{\mathrm{eff}}}{V_s} + 1 \tag{1}$$

$$\varepsilon_{\mathrm{eff},2} \approx -\frac{\Delta \mathrm{BW}}{f_0}\frac{V_{\mathrm{eff}}}{V_s} \tag{2}$$

where $\varepsilon_{\mathrm{eff},1}$ and $\varepsilon_{\mathrm{eff},2}$ are the effective measured dielectric constant and loss, respectively, V_s and V_{eff} are the sample volume and the effective cavity mode volume, respectively, $\Delta \mathrm{BW} = \mathrm{BW}_0 - \mathrm{BW}_s$ and $\Delta f = f_0 - f_s$ are the changes in the measured bandwidth and frequency, and f_0 is the unperturbed resonance frequency. Cavity Q factors of greater than 8000 can be achieved at room temperature with orders of magnitude higher in the super-conducting regime, making the system extremely sensitive to electromagnetic field perturbations at resonance. For the current system, practical measurable differences in the perturbed and unperturbed frequencies and bandwidth of the cylindrical TM_{010} mode at 2.5 GHz ($\varnothing_{\mathrm{cavity}}$ = 92 mm, $\varnothing_{\mathrm{sample}}$ = 2 mm) can be as low as 1 kHz. With a volume scaling ratio of $V_{\mathrm{eff}}/V_s = 0.2898 \times (46\ \mathrm{mm}/1\ \mathrm{mm})^2 = 613.2$, the random errors associated with the dielectric measurement is approximately 2.5×10^{-4}.[40] The dominant contribution to the standard deviation of the measurement is, however, the systematic errors associated with the sample volume and packing density, typically around 5% in previous studies.[40] Materials with a large permittivity produce proportionally large perturbations on the cavity resonances. Previous studies of nano-diamonds with varying impurities have shown large differences in the imaginary part of the complex permittivity in the 2−10 GHz range.[29,40] The surface impurity concentration was controlled through the surface area by varying the particle sizes (from 10 to 1000 nm); hence, the volume of surface impurities is the largest in powders with smaller average particle sizes. The dielectric loss component was observed to being proportional to the sp^2 and disorder carbon concentrations, verified with other techniques. This work did not consider the size and geometric variation of the pure diamond cores and how it affects the observed permittivity. Considering diamond alone, a size-dependent dielectric permittivity may be observed as a consequence of the polarization-related effects from the dangling bonds of the diamond terminations.[42]

We would expect systematic variations in the effective (i.e., measured) permittivity of a powder owing to geometrical factors. Assuming a narrow particle size distribution per sample, there will be large enhancements of local electric fields in the gaps between smaller particles, which give rise to enhanced polarization (owing to the increased external field). This is manifested as an increased effective permittivity of a powder sample consisting of small particles over one of the same volume but comprised of larger particles. The second is the particle shape, which is hard to quantify, but again results in much enhanced local electric fields in regions outside the particles where the surface has a small radius of curvature. The overall trend is for the effective permittivity to increase as the particle size is reduced while maintaining the total volume.

In this research, we mitigate any size- or shape-related effects by using diamond powders of the same average particle size and

DOI: 10.1021/acsomega.7b02000
ACS Omega 2018, 3, 2183−2192

shape, here approximately 710 nm. A simpler method has been proposed to control the sp^2 concentration through vacuum annealing of diamond powders of the same particle size at temperatures from 600 to 1200 °C for a fixed time. The reason why such a large particle size is chosen is due to the fact that there is a much larger volume fraction of sp^3 carbon compared to any other surface impurities (i.e., it being more representative of a purer diamond powder). In this way, trace volumes of surface impurities can be introduced to test the limits of our MCP system. At temperatures greater than 800 °C, partial surface graphitization is expected as is commonly found in the literature, however, most studies tend to use much smaller particle sizes with a much larger initial volume fraction of sp^2 carbon.[19,23,28] The proposed sample method minimizes the geometric dependence explained previously in the MCP measurements, and the resultant differences in the starting and annealed powders will clearly be due to the changes in the material properties. Because there is a firm understanding from the literature about using XPS, STEM−EELS, and Raman spectroscopy to identify the sp^2/sp^3 carbon ratio in carbon-rich materials, they are used as comparison standards for the proposed MCP method to see if the dielectric losses do, in fact, correlate with the sp^2 concentration and not just size as well as to identify the trace sensitivity detection limits.

2. EXPERIMENTAL METHODS

Commercially available sub-micron diamond powder was used throughout (Van Moppes Syndia SYP 0.5-1). The median quoted size of these particles is 710 nm. This powder was annealed in a vacuum chamber at 600, 800, 1000, and 1200 °C for 1 h with the aim to partially graphitize the surfaces of the particles. The powder samples were spread out in a graphite crucible and sat atop a ceramic-topped sample heater, with the chamber evacuated to a pressure of $\leq 10^{-5}$ mbar before annealing, and the samples were left to cool down under vacuum before removing. Field emission scanning electron microscopy (SEM) was carried out after annealing to ensure that the particle size remained constant. The particles were first sputtered with a thin film of gold/platinum alloy (60%:40%) and then measured using a Carl Zeiss 1540xB dual focused ion beam SEM system at 5 kV at 10^{-6} mbar. MCP measurements were conducted using the system detailed in previous nano-diamond studies.[29,39,40] Briefly, the cavity is an aluminum cylindrical cavity resonator (inner $\varnothing_{cavity}$ = 92 mm, h_{cavity} = 40 mm) which has six accessible resonant modes that can be used for complex permittivity measurements at discrete frequencies from 2.5 to 9.4 GHz. The resonant frequency and quality factor (from −3 dB bandwidth) were measured using a Keysight performance network analyser (N5232A). Complex permittivity was obtained using the first-order cavity perturbation equations, which relate the changes in the resonant frequency and quality factor to the dielectric constant and losses, respectively. A schematic of the MCP setup is given in Figure 1. XPS measurements were conducted using a Kratos Axis Ultra DLD system with a monochromatic Al Kα X-ray source operating at 144 W. Initial wide scans were performed with pass energies of 1 eV, and high resolution scans were performed with 0.5 eV. Postprocessing (low pass filtering, spline interpolation, and differentiation) of the Auger spectra was carried out using a program written in National Instruments LabVIEW. Raman spectroscopy was conducted using a Renishaw inVia Reflex with a near-IR laser (λ = 785 nm, ×50 objective and power of 10%). The STEM−EELS measurements

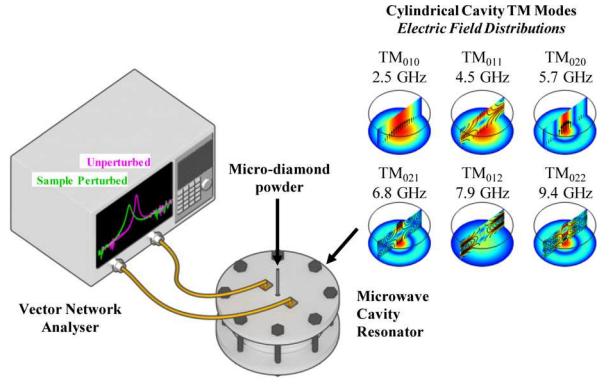

Figure 1. Schematic of the MCP system used in this experiment. Diamond powders were filled into VitroCom quartz tubes ($\varnothing_{sample\ outer\ tube}$ = 2.4 mm, $\varnothing_{sample}$ = 2 mm) and placed into the center of the resonator. The resonant frequency and quality factor (from −3 dB bandwidth) were measured using a vector network analyzer. COMSOL Multiphysics simulations of the electric field distributions of the TM modes used in this study are shown in the top right.

were taken using a FEI Tecnai F30 microscope. The diamond particles were dispersed by an ultrasonic bath into acetone solution, deposited over a lacey carbon film grid, and confirmed using bright-field transmission electron microscopy. Annular dark field STEM micrographs with corresponding EELS spectra were taken for each sample at a number of positions on the particles, with the results presented here serving as a representative measurement.

3. RESULTS AND DISCUSSION

3.1. XPS. The XPS measurements of C 1s and O 1s and the differential of the Auger spectra are shown in Figure 2. The C 1s peak is normally dominated by the contribution from the C−C bonds and is conventionally used as a charge reference at 284.8 eV, as explained earlier. This makes identification of the carbon phases across the different samples challenging. The analysis given here for the C 1s peak assumes that any charge offsets are constant and systematic errors are the same across the measurements (all resultant spectra presented are shifted by 3.08 eV to allow the O 1s peaks to fall around the expected values of 532 eV), again highlighting the referencing limitation of measuring the sp^2/sp^3 carbon ratio using this method. For the starting material, the C 1s spectrum exhibits a convolution of two C peaks, indicative of both sp^3 and surface sp^2 carbon phases.[23] The higher peak situated at around 285 eV is associated with sp^3 carbon, whereas the lower and broader features at around 284 eV are associated with sp^2 carbon. As the diamonds are annealed, the main sp^3 peak becomes less dominant while the lower binding energy peak grows, implicit of an increasing sp^2 concentration on the surface of the particles.[19,23] At 1200 °C, however, the C 1s spectrum is similar to that of the starting material, indicating minimal change in the sp^2 carbon concentration. This is an intriguing result because it has otherwise been reported that increasing annealing temperature tends to increase graphitization.[23,28]

A more robust way of obtaining the sp^2/sp^3 carbon ratio from XPS spectra is to examine the Auger spectrum and obtain the "*D*-value" or "*D*-parameter",[22,43] obtained from the first differential of the C KLL Auger spectrum; the *D*-parameter is taken as the energy difference between the maximum and minimum points. This approach is more appropriate than observing the C 1s shifts because the Auger spectrum does not

DOI: 10.1021/acsomega.7b02000
ACS Omega 2018, 3, 2183−2192

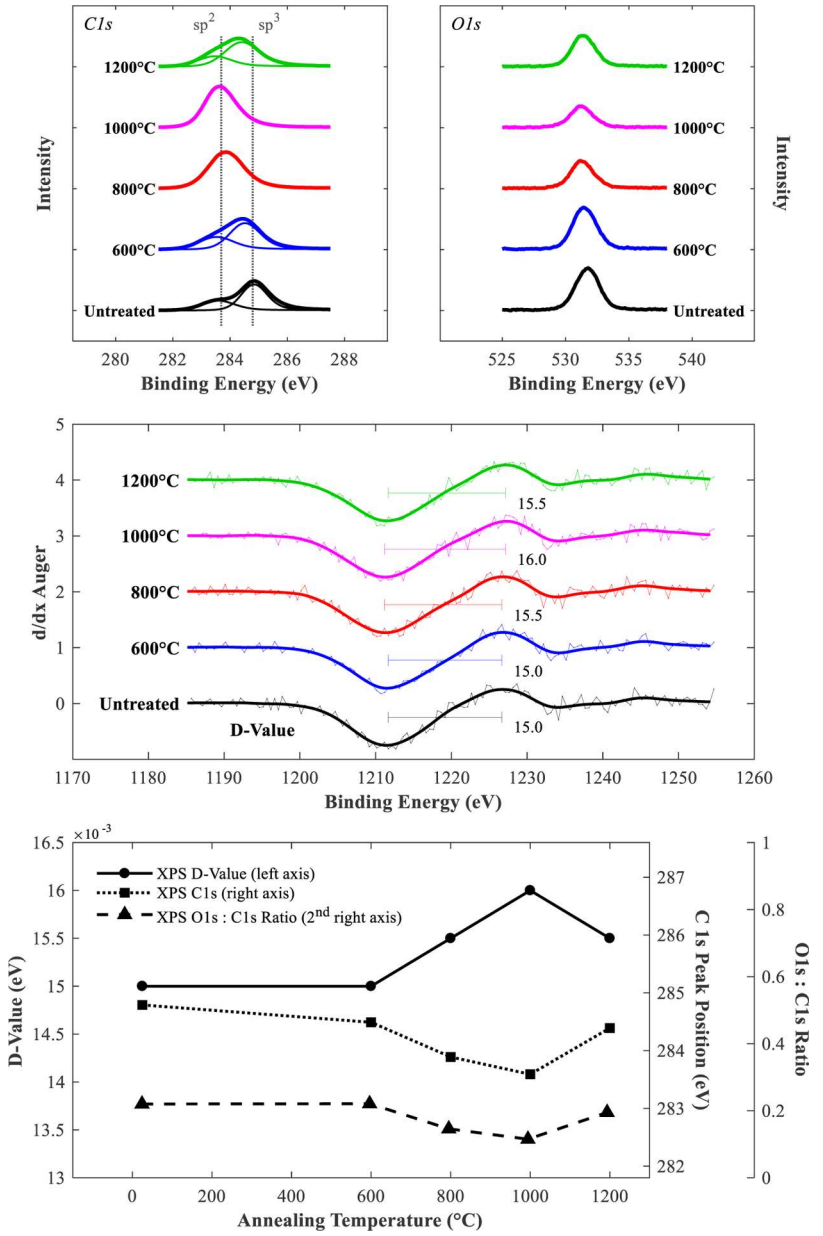

Figure 2. XPS C 1s (top-left), O 1s (top-right), and Auger differential (middle) spectra and change in the *D*-value, C 1s peak position, and O 1s/C 1s ratio as a function of the annealing temperature (bottom). For the C 1s peak, two main peaks are noticed and are attributed to surface sp^3 and sp^2 carbon. The shift of the largest peak toward lower binding energies with annealing temperature is indicative of an increasing sp^2 concentration. The change in the *D*-value (difference in the maximum and minimum of the Auger differential) can be related to the sp^2/sp^3 carbon ratio. The change in the O 1s/C 1s ratio loosely infers hydrogenation through the substitution of oxygen for hydrogen.

require any referencing as it is a differential measurement.[20,24] The differentials of the Auger spectra with the associated *D*-values for each sample are plotted in Figure 2, where similar trends to the C 1s spectra are noticed, with the highest *D*-value observed at 1000 °C. The anticipated rise in the sp^2 concentration with the annealing temperature is again apparent, whereas the anomalous decrease at 1200 °C remains. In addition to the changing sp^2 concentration, the peak O 1s intensity varies in a similar fashion, with the O 1s/C 1s peak ratio loosely indicative of hydrogenation as oxygen is substituted for hydrogen.[44]

3.2. Raman Spectroscopy. The Raman spectroscopy measurements are shown in Figure 3. The strong peak at approximately 1332 cm^{-1} is characteristic of the F_{2g} vibrational mode in sp^3 carbon, hence indicating a large volume fraction of diamond most commonly witnessed for microcrystalline diamond.[31,45] This peak may be obscured by additional D and G bands, associated with the aromatic A_{1g} breathing mode of disordered sp^2 carbon and the E_{2g} bond stretching of sp^2 carbon pairs, respectively, characteristic of graphitic carbon,[46] although in this instance, these bands are of minute intensity as compared to the diamond peak, as shown in Figure 3. Through linear extrapolation of a background baseline at higher wavenumbers, the inset in Figure 3 reveals a broad dispersion of bands around the diamond peak from 1320 to 1600 cm^{-1}, where the D and G bands would be present. This band is most noticeable at the annealing temperature of 1000 °C and diminishes with decreasing temperature, whereas the band of the 1200 °C sample is again less than that at 1000 °C. This is most likely through the formation of small volumes of surface-

DOI: 10.1021/acsomega.7b02000
ACS Omega 2018, 3, 2183−2192

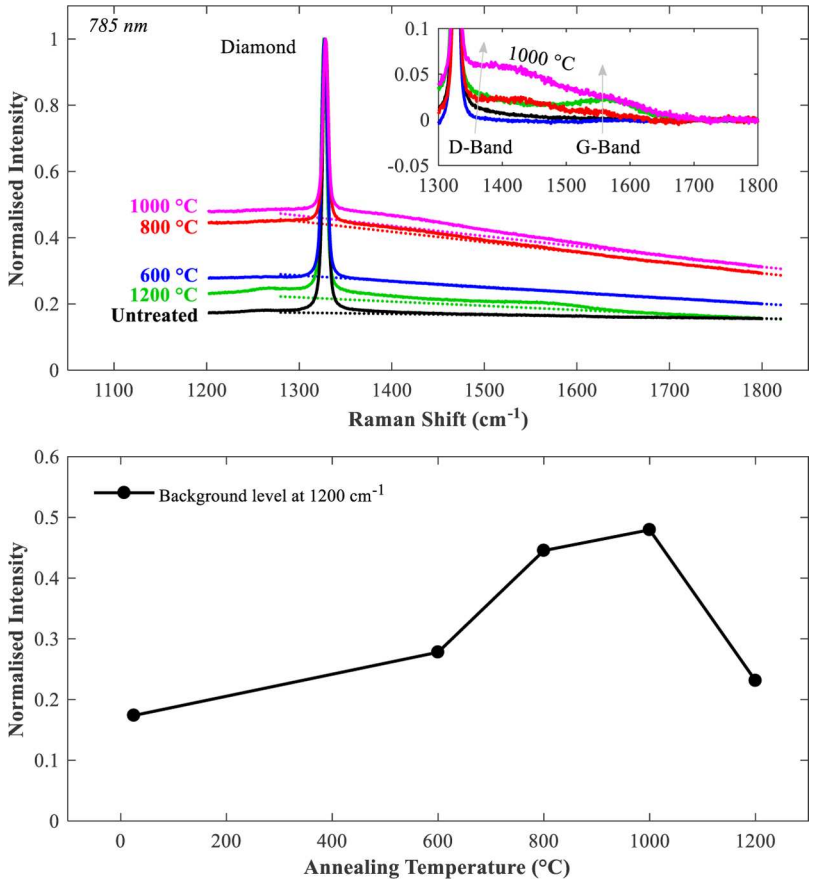

Figure 3. Raman spectra (top) of annealed sub-micron diamond powders using a near-IR laser. All spectra are normalized to the peak value. For analyzing the D and G bands, a baseline background (dotted) is taken through a linear fit in the higher wavenumber region. A clear diamond peak (approximately 1332 cm^{-1}) is evident in all samples, whereas the inset shows the background subtracted spectra in the D and G band regions showing signs of broad D and G bands (around 1320−50 and 1580 cm^{-1}, respectively). This implies small changes in sp^2 carbon with the largest D and G envelope labelled at 1000 °C. In addition, the background PL (bottom), taken as the intensity at 1200 cm^{-1}, is loosely indicative of sample hydrogenation.

disordered sp^2 carbon, albeit too small and sporadically distributed to produce a discernible D or G band. Additionally, the background levels vary among the samples, generally attributed to the photoluminescence (PL) of heavily hydrogenated samples.[46] The varying PL background correlates with the XPS O 1s findings in that as well as any increase in sp^2 carbon, hydrogenation is also taking place to some extent during the annealing process.

3.3. STEM−EELS. The C 1s spectra of the core electrons in the diamond particle are shown for the untreated sample in Figure 4. The edge at approximately 293 eV corresponds to the electron transitions to the σ^* orbitals for sp^3 carbon, which is typically within the range of 289−294 eV.[26,27] Furthermore, the π^* peak, characteristic of sp^2 carbon and usually situated at lower binding energies of around 285 eV, was not found, indicating no measurable sp^2 layer on this particle. Although a survey of the powder sample revealed no evidence of sp^2, that is, not to say that it is not present, it is merely in such low volume concentrations of the bulk powder that it is difficult to identify; whereas XPS is able to identify because of a larger sample probing spot.

For the 600 °C sample, a π^* peak is found at lower binding energies to the σ^* edge on the surface of the particle. At 800 and 1000 °C, the amplitude of the π^* peak significantly increases and decreases again at 1200 °C with position. The trace sp^2 layer thickness can be estimated by varying the position where the spectrum was recorded on the edge of the particle, as shown by the STEM images in Figure 4. Using a modification of the Cuomo expression[25] to compensate that π^* is not really zero on diamond spectra, the sp^2/sp^3 carbon ratio can be obtained as follows

$$\frac{I_{\pi^*}}{I_{\sigma^*}} = 0.54 \times \frac{3x}{4 - x} + 0.067 \quad (3)$$

where I is the peak intensity and x is the sp^2/sp^3 carbon ratio, revealing that the 1000 °C sample has the largest estimated sp^2 thickness. Although these data are conclusive in determining that sp^2 bonding is present on the particle surfaces and varies with the annealing temperature, it is still difficult to quantify this as a representative measurement because it is dependent on the local properties at the point where the spectra are obtained.

3.4. SEM. The SEM measurements are shown in Figure 5. The purpose of these measurements is to demonstrate that the particle size and morphology do not differ greatly as each of the powders are annealed. It is clear that the overall particle size and geometry of the particles do not change, and hence any differences in the XPS, Raman, or MCP measurements will be due to an electromagnetic property of the material. This measurement is important as any significant geometrical changes in the particles can potentially affect the MCP measurements; different particle shapes produce different

DOI: 10.1021/acsomega.7b02000
ACS Omega 2018, 3, 2183−2192

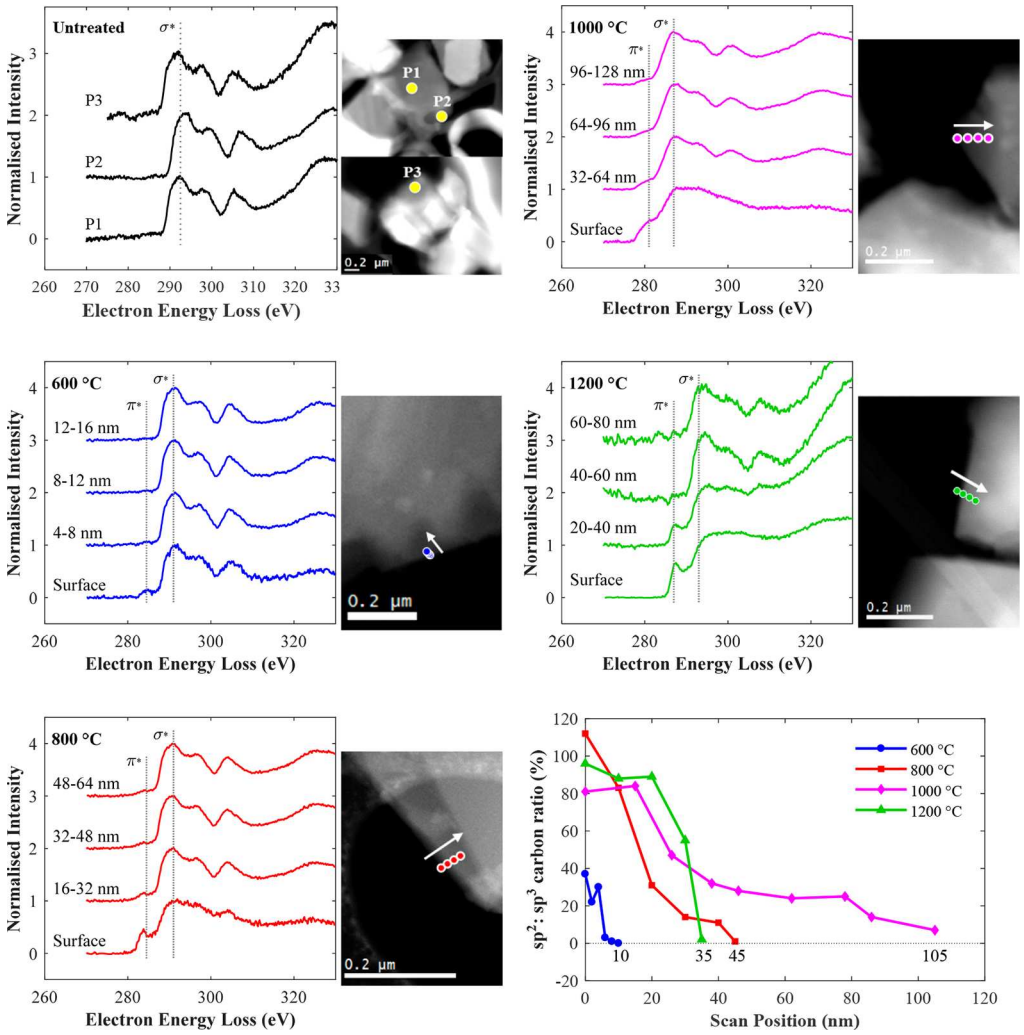

Figure 4. STEM–EELS of the annealed diamond powders at different locations on a particle. The arrow denotes the direction from the surface inward into the particle. No evidence of any sp^2 carbon was found at various points on the initial untreated samples. The annealed samples showed sp^2 carbon layers with approximate thicknesses of 10, 45, 105, and 35 nm for 600, 800, 1000, and 1200 °C, respectively.

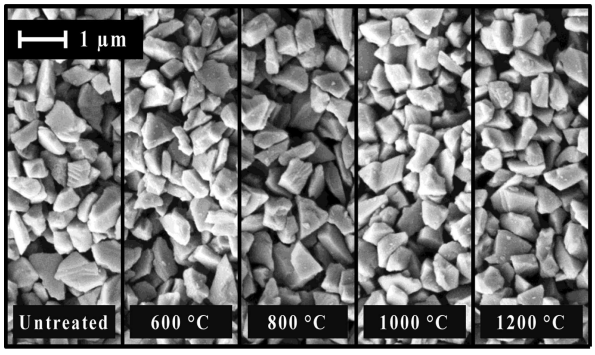

Figure 5. SEM of the annealed diamond powders. There are no drastic changes in the particle size or morphology, thus reducing the geometrical effect on MCP measurements.

electric dipole moments owing to local electric field modifications rather than material property variations, and the observed measurements of the effective (i.e., measured) complex permittivity will vary accordingly.

Thus far, it has been determined that the graphitization of these particles increases with the annealing temperature and the particle geometry does not change, however, the 1200 °C sample does not follow the annealing trend; further discussion on this is in section 4. Having such well-established material properties allows us to make firm correlations with the microwave complex permittivity measurements.

3.5. MCP. The MCP measurements of the effective dielectric constant, dielectric loss, and loss tangent (tan δ) are shown in Figure 6. The first two are calculated using eqns 1 and 2, whereas the loss tangent is simply achieved by taking the quotient of the imaginary and real parts

$$\tan\delta = \frac{\varepsilon''_{\text{eff}}}{\varepsilon'_{\text{eff}}} \approx \frac{-\Delta \text{BW}}{\frac{V_s}{V_{\text{eff}}} f_0 - 2\Delta f} \quad (4)$$

See the reference for more details on the experimental setup.[40] The effective values here mean that no attempt has been made to calculate the *intrinsic* permittivity of the powder material using effective medium theory or by normalizing using the density, as is done in ref 40, as we expect the trends to be visible in the measured data and any changes in the bulk density across the sample to be immeasurable.

The results show that the dielectric constant has minimal correlation with any of the other measurements; in accordance with 1, the dielectric constant is proportional to the shift in the

DOI: 10.1021/acsomega.7b02000
ACS Omega 2018, 3, 2183–2192

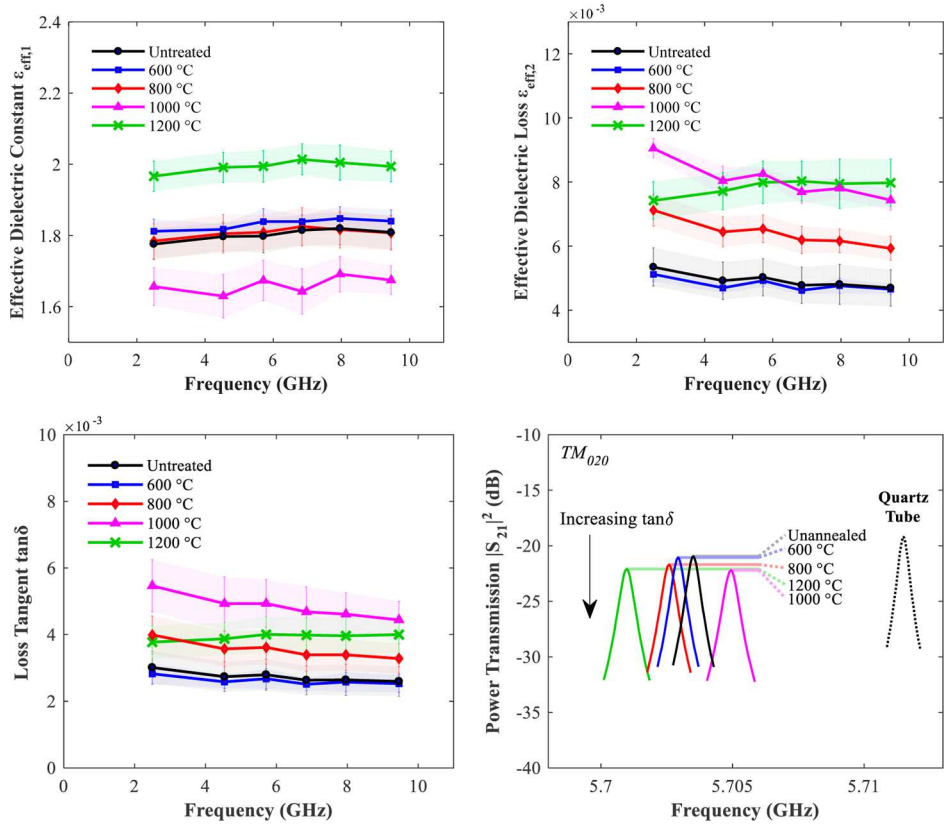

Figure 6. Frequency-dependent effective dielectric constant (top left), loss (top right) and loss tangent (bottom left) from 2.5 to 9.5 GHz, measured using MCP. Error bars are the standard deviation from four measurements of the sub-micron diamond powders. The permittivity is relatively frequency independent, however, a measurable increase in the dielectric loss tangent as the sample is annealed is shown, peaking at 1000 °C and decreasing at 1200 °C. A typical MCP trace (bottom right) of the TM_{020} mode also shows this.

frequency and is depicted in the MCP traces in Figure 6 by the various frequency shifts from the unperturbed measurement (quartz sample container). The loss tangent, however, varies in the same manner as the measurements obtained using XPS (*D*-value and C 1s shift), EELS (C 1s sp^2 carbon layer thickness), and Raman spectroscopy (approximate D- and G-band regions), with an increase from 600 to 1000 °C as well as the unexpected decrease in loss at 1200 °C. Dielectric loss is depicted by an increase in the bandwidth as per 2, though easier to identify on the trace is the loss tangent, which is shown as a decrease in the transmitted power within the resonator (therefore, the sample introduces an insertion loss as it perturbs the electric field of the resonant mode). These findings demonstrate that the measured microwave absorption in these diamond powders is strongly related to an increasing sp^2 carbon volume or sample hydrogenation and is not due to any changes in the size or shape, corroborating results found in previous studies.[29]

The loss tangent is also displayed as a function of the frequency over the 2.5 to 9.4 GHz range in Figure 6. The observed frequency dependence of the loss tangent is minimal; however, there are some small variations in the general trend. The starting powder has the lowest loss tangent with minimal frequency dependence. As the sp^2 concentration increases, a negative gradient with the frequency starts to emerge, most prominently at 1000 °C. The general increase in tan δ is related to the volume increase in non-diamond carbon impurities, and an inverse frequency dependence can be modelled as an enhancement in the long-range, free-charge conduction; as described in the previous work, we expect that $\tan\delta \approx \sigma_{static}/\omega\varepsilon_0\varepsilon_{eff,1}$, where ε_0 is the free space permittivity and σ_{static} is the long-range, free-charge conductivity.[24] The presented data here are not significant enough to be attributed to any noticeable long-range charge conduction. It is worth noting here that the standard deviation error bars denote error between the different prepared samples and not across the band. The overall frequency-dependent characteristic was found to be similar among all samples; thus, the error bars are more indicative of absolute offsets in the whole data.

4. DISCUSSION

The most pertinent outcome of these experiments is that the MCP dielectric loss tangent correlates with all other measured findings from two contributions, sp^2 carbon concentration and the extent to which the sample is hydrogenated.

For the case of a varying sp^2 carbon concentration, the unclear Raman results must first be discussed. Initially, the absence of clear D and G bands in the Raman spectra suggests that graphitization has not occurred at any of the temperatures, especially because the excitation wavelength of the laser is in the near-IR region and is therefore particularly sensitive to the presence of sp^2 carbon.[30] However, this would disregard all of the XPS and EELS measurements, which suggest that the sp^2/sp^3 carbon ratio is changing. A more reasonable explanation is that the vacuum annealing process introduces small volumes of sp^2 carbon impurities, spuriously distributed on the diamond crystallites, as verified by EELS. These volumes are so small that discernible D and G bands cannot be detected, but instead

DOI: 10.1021/acsomega.7b02000
ACS Omega 2018, 3, 2183−2192

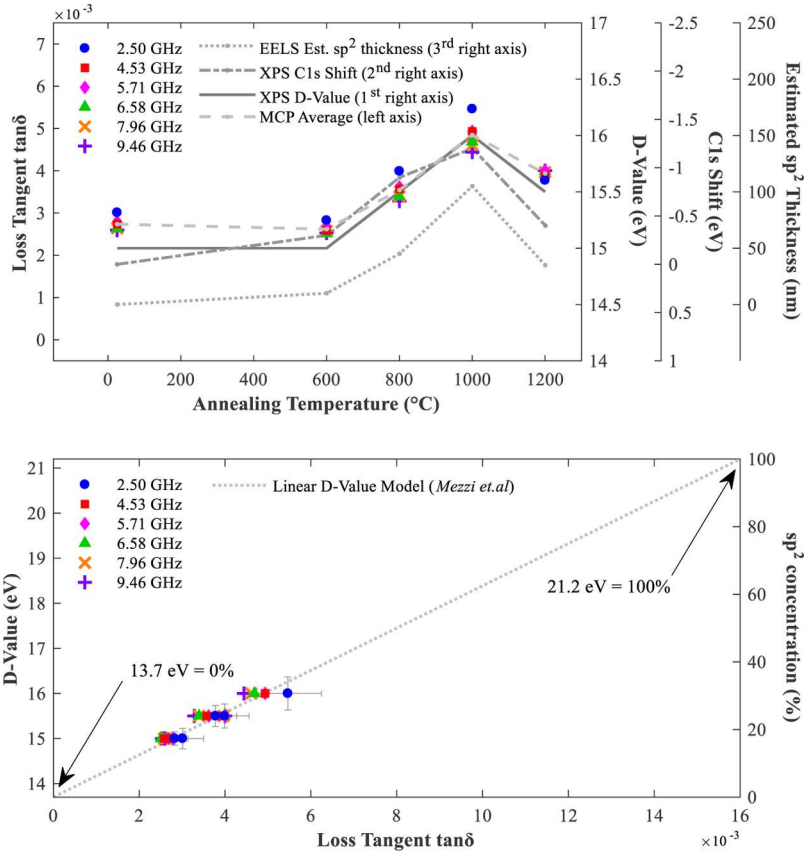

Figure 7. MCP measurements of the dielectric loss tangent of the annealed diamond particles with the XPS and EELS measurements (top). Correlation of MCP and XPS (bottom) is shown with the second *y* axis labelled as sp^2 concentration because this is linearly related to the *D*-value (using 0% at 13.7 eV and 100% as 21.2 eV[24]). Error bars in the *x* direction indicate the standard deviation for the sample measurement at 2.5 GHz, whereas the *y* direction shows these same errors translated onto the sp^2 concentration axis, thereby showing the error in the measurement of sp^2 concentration using the MCP approach.

a broad feature encompassing both of them is measured. An indication of sp^2/sp^3 carbon concentration from Raman is generally given through either the peak ratio of the G band and the diamond peak or a ratio of the integration of their respective areas.[45] Through observation, it is clear that the broad feature in Figure 3 inset between 1300 and 1600 cm^{-1} peaks at 1000 °C, however, the accuracy is heavily dependent upon the arbitrary classification of the Raman baseline level. For the sizes of the particles used here, they are much larger than those used in other annealing studies (5−50 nm range[28]), and so the sp^2 growth rate is dramatically slower, producing a much smaller volume fraction of sp^2 carbon. The sensitivity of Raman spectroscopy in this case is heavily weighted toward large volumes of periodic and crystalline contributions. Typical penetration depths of near-IR lasers are on the order of micrometers, whereas XPS and EELS are point surface techniques with probing depths in the nanometer range, making Raman spectroscopy more sensitive to the bulk particle. This explains why both XPS and EELS measurements are more capable of detecting a changing sp^2/sp^3 carbon concentration in this sample set. However, MCP also probes the bulk, but unlike Raman spectroscopy, it is much less sensitive to the insulating crystalline diamond contribution, and hence a correlation between the sp^2 indicators from XPS and EELS and MCP is found.

The counter argument for the observed changes in the MCP results is in the sample hydrogenation. This may have occurred from water vapor present on the chamber walls prior to the annealing stages, which is fully conceivable as per vacuum annealing experiments by Ginés et al.[47] As is shown in the XPS O 1s/C 1s ratio and the Raman rising PL background, these hydrogenation indicators show that with increasing annealing temperature, the sample is further hydrogenated until it saturates at 1000 °C and decreases at 1200 °C. Hence, a correlation similar to that of the sp^2 indicators is obtained, and one could argue that the measured increase in the microwave loss tangent is a consequence of hydrogenation, namely hole conduction from the ambient surface conduction phenomenon in hydrogenated diamond.[44] Hydrogenated diamond has been demonstrated to drastically affect the dc conductivity of pure diamond, decreasing the dc resistivity from 10^7 to 10^5 Ω cm, and thus σ = 1 mS/m.[44] The low-frequency long-range conductivity of the untreated powder has been measured in our previous work[40] giving a similar value, implying that these samples are already hydrogenated before treatment, congruent with the initial PL background in Figure 3. Because both sp^2 carbon and hydrogenation indicators are present, the question is, *which mechanism is most likely to have a larger impact on the microwave dielectric properties?*

In this work, we assume that the electrical properties of sp^2 carbon are far superior to that of hole transport in hydrogenated diamond. This is a reasonable hypothesis, graphitic carbon is known to have a very high dielectric loss tangent in the microwave frequency range and so microwave

DOI: 10.1021/acsomega.7b02000
ACS Omega 2018, 3, 2183−2192

measurement systems are highly sensitive to this material.[48] This is a significant result, with the correlation between the *D*-value and loss tangent shown in Figure 7. For the XPS *D*-value, a simple linear model can be used to quantify the surface sp^2 carbon concentration in trace amounts, giving a small percentage increase in sp^2 carbon from approximately 17−31% after annealing, as shown in Figure 7. With MCP plotted against this, tan δ of 0.016 is extrapolated to 100%. The error bars in Figure 7 show that the sp^2 concentration can be resolved with a maximum standard deviation of ±5%. However, it must be made clear that the linear model given in Figure 7 is not linear at higher concentrations than those measured here (less than approximately 31%) because applying it to previously measured nano-diamonds yields sp^2 concentrations of greater than 200%.[40] Comparing the MCP standard deviation of ±5% with XPS, fine scans achieved with 0.1 eV resolution translate to a conservative 2% sensitivity for a 0−100% sp^2 range of 13.7−21.2 eV.[24] Whereas XPS in this regard is more sensitive than the MCP system used here, the setup of MCP is much simpler. The MCP system can also be improved by designing a higher quality factor cavity resonator; for example, by increasing the conductivity of the cavity metal by using copper instead of the currently used aluminum cavity and by allowing greater changes in the bandwidth to be measured for tan δ measurements.

Regarding the 1200 °C sample, which did not exhibit as much sp^2 carbon as the 1000 °C sample, it has seemingly shown the completely opposite result to what was anticipated; its inferred sp^2 concentration from XPS, EELS, and MCP measurements did not increase at temperatures higher than 1000 °C, the Raman PL background reduced to values similar to the starting material, and its dielectric loss characteristic as a function of frequency marginally increases, as opposed to decreasing as per the inverse frequency dependence in the long-range conduction model.[40] The observed increase in the dielectric loss with increasing frequency is intriguing, as conventionally, one would only observe such increases when a material's permittivity approaches dielectric relaxation. However, this is generally complemented with a decrease in the real part of the permittivity with frequency, which is not observed. One explanation for the anomalous 1200 °C sample is related to the water vapor on the chamber walls at the start of the experiment in that the sample is saturated with the desorbed hydrogen at 1000 °C to the point that at a higher temperature of 1200 °C, this hydrogenation facilitates in etching off the sp^2 bonding. The sp^2 carbon growth kinetics is less reported for diamonds approaching the micrometer size as opposed to those readily used to synthesize nano-sized onionlike carbon (<10 nm).[28,49,50] Regardless of the obscure growth kinetics for this diamond sample at this temperature, the XPS, Raman, EELS, and MCP results are all correlated, and so this discrepancy does not affect the overall conclusions of this work.

5. CONCLUSIONS

The MCP measurements shown here demonstrate that trace amounts of sp^2 carbon impurities on sub-micron-sized diamonds can be detected with standard deviation errors as low as ±5%. The microwave loss tangent demonstrates a linear relationship with the sp^2 concentration, with surface sp^2/sp^3 carbon ratios of up to 31% obtained using the XPS *D*-value. Additional indicators also verified the presence of a varying sp^2 carbon ratio, including changes in the XPS C 1s spectra, EELS C 1s spectra, and a small and broad region encompassing the D and G bands in the Raman spectra. In addition, varying hydrogenation was detected in the particles through a rising PL background in Raman and a varying XPS O 1s/C 1s ratio. This needs further investigation, in particular, at a fixed sp^2 carbon concentration, to understand its effect on MCP measurements. Practically, this work demonstrates potentially new avenues in materials science using microwave dielectric spectroscopy for quality control in the production of sub-micron-sized diamond powders. However, when used in isolation, one must exercise caution because it does not identify phases within a material and should be used in complement to others.

AUTHOR INFORMATION

Corresponding Author

*E-mail: cuencaj@cardiff.ac.uk (J.A.C.).

ORCID

Jerome Alexander Cuenca: 0000-0003-1370-1167

Soumen Mandal: 0000-0001-8912-1439

David John Morgan: 0000-0002-6571-5731

Notes

The authors declare no competing financial interest.

ACKNOWLEDGMENTS

We thank Dr. Emmanuel Brousseau for technical assistance with obtaining the SEM images of the annealed diamond powders. We also thank Dr. Joel Loveridge for preliminary NMR measurements.

REFERENCES

(1) Aleksov, A.; Kubovic, M.; Kasu, M.; Schmid, P.; Grobe, D.; Ertl, S.; Schreck, M.; Stritzker, B.; Kohn, E. Diamond-Based Electronics for RF Applications. *Diamond Relat. Mater.* **2004**, *13*, 233−240.

(2) Aleksov, A.; Kubovic, M.; Kaeb, N.; Spitzberg, U.; Bergmaier, A.; Dollinger, G.; Bauer, T.; Schreck, M.; Stritzker, B.; Kohn, E. Diamond Field Effect Transistors—Concepts and Challenges. *Diamond Relat. Mater.* **2003**, *12*, 391−398.

(3) Gurbuz, Y.; Esame, O.; Tekin, I.; Kang, W. P.; Davidson, J. L. Diamond Semiconductor Technology for RF Device Applications. *Solid-State Electron.* **2005**, *49*, 1055−1070.

(4) Chow, E. K.; Zhang, X.-Q.; Chen, M.; Lam, R.; Robinson, E.; Huang, H.; Schaffer, D.; Osawa, E.; Goga, A.; Ho, D. Nanodiamond Therapeutic Delivery Agents Mediate Enhanced Chemoresistant Tumor Treatment. *Sci. Transl. Med.* **2011**, *3*, 73ra21.

(5) Kaur, R.; Badea, I. Nanodiamonds as Novel Nanomaterials for Biomedical Applications: Drug Delivery and Imaging Systems. *Int. J. Nanomed.* **2013**, *8*, 203−220.

(6) Wang, Z.; Tian, Z.; Dong, Y.; Li, L.; Tian, L.; Li, Y.; Yang, B. Nanodiamond-Conjugated Transferrin as Chemotherapeutic Drug Delivery. *Diamond Relat. Mater.* **2015**, *58*, 84−93.

(7) Xiao, J.; Duan, X.; Yin, Q.; Zhang, Z.; Yu, H.; Li, Y. Nanodiamonds-Mediated Doxorubicin Nuclear Delivery to Inhibit Lung Metastasis of Breast Cancer. *Biomaterials* **2013**, *34*, 9648−9656.

(8) Kulha, P.; Kromka, A.; Babchenko, O.; Vanecek, M.; Husak, M.; Williams, O. A.; Haenen, K. Nanocrystalline Diamond Piezoresistive Sensor. *Vacuum* **2009**, *84*, 53−56.

(9) Kusterer, J.; Lüker, A.; Herfurth, P.; Men, Y.; Ebert, W.; Kirby, P.; O'Keefe, M.; Kohn, E. Piezo-Actuated Nanodiamond Cantilever Technology for High-Speed Applications. *Diamond Relat. Mater.* **2008**, *17*, 1429−1433.

(10) Shenderova, O.; Gruen, D. *Ultrananocrystalline Diamond*; Shenderova, O., Gruen, D., Eds.; William Andrew Publishing: New York, 2006; pp 291−326.

(11) Hsin, Y. L.; Chu, H.-Y.; Jeng, Y.-R.; Huang, Y.-H.; Wang, M. H.; Chang, C. K. In Situ de-Agglomeration and Surface Functionalization

DOI: 10.1021/acsomega.7b02000
ACS Omega 2018, 3, 2183−2192

of Detonation Nanodiamond, with the Polymer Used as an Additive in Lubricant Oil. *J. Mater. Chem.* **2011**, *21*, 13213−13222.
(12) Costa, G. C. C.; Shenderova, O.; Mochalin, V.; Gogotsi, Y.; Navrotsky, A. Thermochemistry of Nanodiamond Terminated by Oxygen Containing Functional Groups. *Carbon* **2014**, *80*, 544−550.
(13) Mochalin, V. N.; Shenderova, O.; Ho, D.; Gogotsi, Y. The Properties and Applications of Nanodiamonds. *Nat. Nanotechnol.* **2011**, *7*, 11−23.
(14) Krueger, A.; Lang, D. Functionality Is Key: Recent Progress in the Surface Modification of Nanodiamond. *Adv. Funct. Mater.* **2012**, *22*, 890−906.
(15) Williams, O. A. *Nanodiamond: Nanoscience*; Royal Society of Chemistry, 2014.
(16) Pichot, V.; Comet, M.; Fousson, E.; Baras, C.; Senger, A.; Le Normand, F.; Spitzer, D. An Efficient Purification Method for Detonation Nanodiamonds. *Diamond Relat. Mater.* **2008**, *17*, 13−22.
(17) Osswald, S.; Yushin, G.; Mochalin, V.; Kucheyev, S. O.; Gogotsi, Y. Control of sp^2/sp^3 Carbon Ratio and Surface Chemistry of Nanodiamond Powders by Selective Oxidation in Air. *J. Am. Chem. Soc.* **2006**, *128*, 11635−11642.
(18) Kaciulis, S. Spectroscopy of Carbon: From Diamond to Nitride Films. *Surf. Interface Anal.* **2012**, *44*, 1155−1161.
(19) Petit, T.; Arnault, J.-C.; Girard, H. A.; Sennour, M.; Bergonzo, P. Early Stages of Surface Graphitization on Nanodiamond Probed by X-Ray Photoelectron Spectroscopy. *Phys. Rev. B: Condens. Matter Mater. Phys.* **2011**, *84*, 233407.
(20) Fujimoto, A.; Yamada, Y.; Koinuma, M.; Sato, S. Origins of sp^3C Peaks in C 1s X-Ray Photoelectron Spectra of Carbon Materials. *Anal. Chem.* **2016**, *88*, 6110−6114.
(21) Leung, T. Y.; Man, W. F.; Lim, P. K.; Chan, W. C.; Gaspari, F.; Zukotynski, S. Determination of the sp^3/sp^2 Ratio of a-C:H by XPS and XAES. *J. Non-Cryst. Solids* **1999**, *254*, 156−160.
(22) Speranza, G.; Laidani, N. Measurement of the Relative Abundance of sp^2 and sp^3 Hybridised Atoms in Carbon-Based Materials by XPS: A Critical Approach. Part II. *Diamond Relat. Mater.* **2004**, *13*, 451−458.
(23) Xie, F. Y.; Xie, W. G.; Gong, L.; Zhang, W. H.; Chen, S. H.; Zhang, Q. Z.; Chen, J. Surface Characterization on Graphitization of Nanodiamond Powder Annealed in Nitrogen Ambient. *Surf. Interface Anal.* **2010**, *42*, 1514−1518.
(24) Mezzi, A.; Kaciulis, S. Surface Investigation of Carbon Films: From Diamond to Graphite. *Surf. Interface Anal.* **2010**, *42*, 1082−1084.
(25) Cuomo, J. J.; Doyle, J. P.; Bruley, J.; Liu, J. C. Sputter Deposition of Dense Diamond-like Carbon Films at Low Temperature. *Appl. Phys. Lett.* **1991**, *58*, 466−468.
(26) Duan, X.; Ao, Z.; Li, D.; Sun, H.; Zhou, L.; Suvorova, A.; Saunders, M.; Wang, G.; Wang, S. Surface-Tailored Nanodiamonds as Excellent Metal-Free Catalysts for Organic Oxidation. *Carbon* **2016**, *103*, 404−411.
(27) Aramesh, M.; Fox, K.; Lau, D. W. M.; Fang, J.; Ostrikov, K.; Prawer, S.; Cervenka, J. Multifunctional Three-Dimensional Nanodiamond-Nanoporous Alumina Nanoarchitectures. *Carbon* **2014**, *75*, 452−464.
(28) Panich, A. M.; Shames, A. I.; Sergeev, N. A.; Olszewski, M.; McDonough, J. K.; Mochalin, V. N.; Gogotsi, Y. Nanodiamond Graphitization: A Magnetic Resonance Study. *J. Phys.: Condens. Matter* **2013**, *25*, 245303.
(29) Cuenca, J. A.; Thomas, E.; Mandal, S.; Williams, O.; Porch, A. Microwave Determination of sp^2 Carbon Fraction in Nanodiamond Powders. *Carbon* **2015**, *81*, 174−178.
(30) Wagner, J.; Wild, C.; Koidl, P. Resonance Effects in Raman Scattering from Polycrystalline Diamond Films. *Appl. Phys. Lett.* **1991**, *59*, 779−781.
(31) Prawer, S.; Nemanich, R. J. Raman Spectroscopy of Diamond and Doped Diamond. *Philos. Trans. R. Soc., A* **2004**, *362*, 2537−2565.
(32) May, P. W.; Smith, J. A.; Rosser, K. N. 785 Nm Raman Spectroscopy of CVD Diamond Films. *Diamond Relat. Mater.* **2008**, *17*, 199−203.
(33) Su, S.; Li, J.; Kundrát, V.; Abbot, A. M.; Ye, H. Hydrogen-Passivated Detonation Nanodiamond: An Impedance Spectroscopy Study. *Diamond Relat. Mater.* **2012**, *24*, 49−53.
(34) Bevilacqua, M.; Chaudhary, A.; Jackman, R. B. The Influence of Ammonia on the Electrical Properties of Detonation Nanodiamond. *J. Appl. Phys.* **2009**, *106*, 123704.
(35) Gavrilkin, S. M.; Poyarkov, K. B.; Matseevich, B. V.; Batsanov, S. S. Dielectric Properties of Diamond Powder. *Inorg. Mater.* **2009**, *45*, 980−981.
(36) Clark, N.; Jones, N.; Porch, A. Measurement of Average Particle Size in Metal Powders by Microwave Cavity Perturbation in the Magnetic Field. *Sens. Actuators, A* **2017**, *259*, 137−143.
(37) Cuenca, J. A.; Slocombe, D. R.; Porch, A. Temperature Correction for Cylindrical Cavity Perturbation Measurements. *IEEE Trans. Microwave Theory Tech.* **2017**, *65*, 2153−2161.
(38) Jones, M. O.; Hartley, J.; Porch, A. Simultaneous Neutron Diffraction and Microwave Dielectric Characterisation of Ammine Materials—a Non-Destructive, Non-Contact Characterisation Tool for Determining Ammonia Content in Solids. *Phys. Chem. Chem. Phys.* **2016**, *18*, 23340−23347.
(39) Slocombe, D.; Porch, A.; Bustarret, E.; Williams, O. A. Microwave Properties of Nanodiamond Particles. *Appl. Phys. Lett.* **2013**, *102*, 244102.
(40) Cuenca, J. A.; Thomas, E.; Mandal, S.; Williams, O.; Porch, A. Investigating the Broadband Microwave Absorption of Nanodiamond Impurities. *IEEE Trans. Microwave Theory Tech.* **2015**, *63*, 4110−4118.
(41) Cuenca, J. A.; Bugler, K.; Taylor, S.; Morgan, D.; Williams, P.; Bauer, J.; Porch, A. Study of the Magnetite to Maghemite Transition Using Microwave Permittivity and Permeability Measurements. *J. Phys.: Condens. Matter* **2016**, *28*, 106002.
(42) Batsanov, S. S. On the Size-Effect in the Dielectric Permittivity of Solids. *J. Phys. Chem. Solids* **2016**, *91*, 90−92.
(43) Speranza, G.; Laidani, N. Measurement of the Relative Abundance of sp^2 and sp^3 Hybridised Atoms in Carbon Based Materials by XPS: A Critical Approach. Part I. *Diamond Relat. Mater.* **2004**, *13*, 445−450.
(44) Kondo, T.; Neitzel, I.; Mochalin, V. N.; Urai, J.; Yuasa, M.; Gogotsi, Y. Electrical Conductivity of Thermally Hydrogenated Nanodiamond Powders. *J. Appl. Phys.* **2013**, *113*, 214307.
(45) Ramamurti, R.; Shanov, V.; Singh, R. N.; Mamedov, S.; Boolchand, P. Raman Spectroscopy Study of the Influence of Processing Conditions on the Structure of Polycrystalline Diamond Films. *J. Vac. Sci. Technol., A* **2006**, *24*, 179−189.
(46) Casiraghi, C.; Ferrari, A. C.; Robertson, J. Raman Spectroscopy of Hydrogenated Amorphous Carbons. *Phys. Rev. B: Condens. Matter Mater. Phys.* **2005**, *72*, 085401.
(47) Ginés, L.; Mandal, S.; Ashek-I-Ahmed; Cheng, C.-L.; Sow, M.; Williams, O. A. Positive Zeta Potential of Nanodiamonds. *Nanoscale* **2017**, *9*, 12549−12555.
(48) Hotta, M.; Hayashi, M.; Lanagan, M. T.; Agrawal, D. K.; Nagata, K. Complex Permittivity of Graphite, Carbon Black and Coal Powders in the Ranges of X-Band Frequencies (8.2 to 12.4 GHz) and between 1 and 10 GHz. *ISIJ Int.* **2011**, *51*, 1766−1772.
(49) Tomita, S.; Burian, A.; Dore, J. C.; LeBolloch, D.; Fujii, M.; Hayashi, S. Diamond Nanoparticles to Carbon Onions Transformation: X-Ray Diffraction Studies. *Carbon* **2002**, *40*, 1469−1474.
(50) Zou, Q.; Wang, M.; Lv, B.; Li, Y.; Yu, H.; Zou, L.; Zhao, Y. Fabrication of Onion-like Carbon Using Nanodiamond by Annealing at Lower Temperature and Vacuum. *J. Wuhan Univ. Technol., Mater. Sci. Ed.* **2009**, *24*, 935−939.

DOI: 10.1021/acsomega.7b02000
ACS Omega 2018, 3, 2183−2192